

# Accretion Stream Mapping of HU Aquarii

Sonja Vrielmann<sup>1\*</sup>, Axel D. Schwope<sup>2</sup>

<sup>1</sup>*Department of Astronomy, University of Cape Town, Private Bag, Rondebosch, 7700, South Africa*

<sup>2</sup>*Astrophysikalisches Institut Potsdam, An der Sternwarte 16, 14482 Potsdam, Germany*

28 November 2018

## ABSTRACT

We present a new mapping algorithm, the *Accretion Stream Mapping (ASM)* which uses the full phase-coverage of a light curve to derive spatially resolved intensity distributions along the accretion stream in magnetic cataclysmic variables of AM Herculis type (polars). The surface of the accretion stream is approximated as a duodecadon shaped tube. After successfully testing this method on artificial data we applied it to emission line light curves of  $H\beta$ ,  $H\gamma$  and  $\text{He II } \lambda 4686$  of the bright eclipsing polar HU Aqr. We find Hydrogen and Helium line emission bright in the threading region of the stream where the stream couples onto magnetic field lines. It is particularly interesting, that the stream is bright on the irradiated side, facing the white dwarf, which highlights the interplay of collisional and radiative excitation/ionization.

**Key words:** binaries: eclipsing – cataclysmic variables – accretion stream – stars: HU Aqr

## 1 INTRODUCTION

The strong magnetic field in cataclysmic binaries of AM Herculis type, so called polars, keeps both stars in synchronous rotation (with a few exceptions having slightly asynchronously rotating white dwarfs), leads to intense cyclotron radiation from the small accretion spots at the magnetic poles of the white dwarf and prevents the formation of an accretion disc. Instead, stellar matter is transferred via an accretion stream from the late-type main sequence star (the secondary) to the white dwarf.

In the basic picture the stream leaves the secondary via Roche-lobe overflow at the inner Lagrangian point  $L_1$  to initially follow a ballistic trajectory down to some radius where the magnetic pressure overcomes the ram pressure (Liebert & Stockman 1985). In this interaction region the growth of plasma instabilities of Rayleigh-Taylor and Kelvin-Helmholtz type leads to a break-up of the stream resulting in a fine rain of small droplets which follow magnetic field lines and are finally accreted onto the white dwarf (Hameury et al. 1986).

This scenario was observationally confirmed in its basic features by Doppler tomography of bright emission lines revealing a ballistic stream (Schwope, Mantel & Horne 1997; SMH97 henceforth) and by the occurrence of X-ray absorption dips originating in the magnetic part of the stream (e.g. Watson et al. 1989). X-ray emission from the stream

due to dissipative heating in the interaction region was predicted to occur (Liebert & Stockman 1985), but never observed. Doppler tomography also revealed the existence of an accretion curtain raising from footpoints everywhere along the ballistic accretion stream.

Observationally, the question of locating the stream (or streams), the accretion curtain and the brightness distribution along these structures was pushed forward by mapping experiments of emission line and continuum radiation in two eclipsing systems, HU Aqr and UZ For (Hakala 1995, Harrop-Allin et al. 1998, 1999a, 1999b, Heerlein et al. 1999, Kube et al. 2000, Sohl & Wynn 1999, Vrielmann & Schwope 1999). Hakala and Harrop-Allin et al. were using broad-band UBVR eclipse light curves of HU Aqr in order to derive the brightness distribution along the stream. They tried different stream geometries, a single stream bound to the orbital plane or a stream with a ballistic part and accretion down to one or two poles. The major drawback using this type of input data are the contributions of various radiation components (i.e. the stream, the white dwarf and the accretion spot with photospheric and cyclotron emission) with different and partly unknown angular characteristics. Their advantage is the high time resolution and good signal-to-noise ratio of the broad-band data.

Kube et al. were using a similar geometry and optimization method as the former authors, for the case of UZ For. They mapped the brightness distribution of the  $\text{C IV } \lambda 1550$  emission line extracted from high-time low-spectral resolution observations with the HST/FOS around eclipse phase.

\* Send offprint requests to: sonja@penguin.ast.uct.ac.za

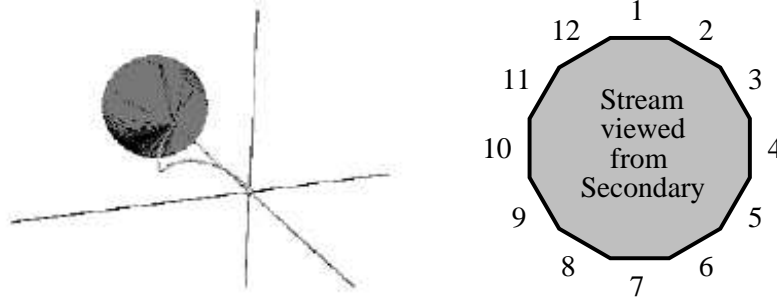


**Figure 1.** *Left:* The geometry of the system. Shown are the secondary star in the back, the accretion stream and the white dwarf in a perspective view at binary phase  $\simeq 0.55$ . The coordinate axis is centred in the white dwarf. *Right:* The duodecagon shaped stream crosssection as viewed from the inner Lagrangian point  $L_1$  on the secondary.

This approach has the advantage of eliminating the angle-dependent continuum emission from the accretion spot.

Heerlein et al. and Sohl & Wynn modelled the full, complex emission line profile of He II  $\lambda 4686$  in HU Aqr obtained with full phase coverage and high time and spectral resolution when the system was in a high accretion state. The resulting maps are constrained by the velocity distribution observed at all phases rather than by the brightness variations during eclipses. Hence, these methods give complementary information to the eclipse mapping methods.

Here, we present a new approach to derive the brightness distribution along the accretion stream in HU Aqr taking the three-dimensionality of the stream into account. We analyse emission line light curves of Balmer  $H\beta$ ,  $H\gamma$ , and He II  $\lambda 4686$ , obtained with full phase-resolution and subtracted reprocessed radiation from the secondary star (SMH97). Schwope et al. have shown that the stream emits differently on its irradiated (inner) side than on its non-irradiated (outer) side. We, therefore, map in our model the observed brightness distribution on an accretion stream approximated as an opaque tube. Some early results were presented in Vrielmann & Schwope (1999).

The structure of the paper is the following: in Sect. 2 we describe the data used for the mapping method; Sections 3.1 and 3.2 outline our model and assumptions; the application to artificial data is described in Sect. 3.3; and to observed data in Sect. 3.4. The paper is closed by a discussion section 4, where our results are compared to those of other groups.

## 2 THE DATA

Spectroscopy of HU Aqr with high time and spectral resolution was performed in the night August 17/18, 1993, with the double-beam spectrograph TWIN at the 3.5m telescope on Calar Alto, Spain. Simultaneous high-speed UBVRI photometry was performed at the 2.2m telescope, only 300 m away. The photometry allowed us to reduce trailing errors and seeing variability in the spectroscopic data. The individual reduction steps are described in SMH97, where a detailed analysis of the emission lines, in particular He II  $\lambda 4686$ , is presented.

For our present analysis we use the light curves in integrated light of  $H\beta$ ,  $H\gamma$ , and He II  $\lambda 4686$ . Since in our present study we are interested only in emission originating from the accretion stream, we corrected the integral light curve

for the emission originating on the irradiated surface of the secondary. For that purpose we used the Gaussian deconvolution of the He II  $\lambda 4686$  line (SMH97, Fig. 7), smoothed the observed asymmetric light curve of the narrow emission line from the secondary star and subtracted it from the integrated light curve. We used the same correction function, appropriately scaled, for all three lines concerned. The remaining emission is regarded to originate solely from the accretion stream; the resulting light curves are shown in Fig. 5. We will discuss below (Sect. 3.4) the effects of uncertainties of the correction function.

## 3 ACCRETION STREAM MAPPING, ASM

### 3.1 The method

The *Accretion Stream Mapping* method, henceforth called ASM, is based on classical *Eclipse Mapping* of accretion discs in eclipsing cataclysmic variables (Horne 1985). This classical algorithm is used to reconstruct intensity distributions in the accretion disc by fitting the eclipse profile and applying a maximum entropy algorithm in order to retrieve a unique solution for this otherwise ill-conditioned problem.

Two major differences which are implemented in ASM with respect to the classical *Eclipse Mapping* are: (a) the disc geometry is replaced by a stream geometry; (b) since the accretion stream eclipses *itself*, we use the full orbital light curve, instead of a short data interval centred on eclipse. In principle, we are not confined to eclipsing systems (i.e. systems which show an eclipse of the white dwarf by the secondary; see also Section 3.3.2), however, they provide us with valuable information in form of ingress and egress profiles in the light curve. Therefore, we use data of the eclipsing polar HU Aqr.

As a consistency check for our solution we use B-band photometry with high time resolution (0.5 sec) around eclipse for comparison. Our approach assumes that emission from the stream is completely optically thick, the observed brightness variation is then solely due to projection and occultation of stream pixels and not to variable optical depth.

The stream is modelled as a tube with twelve sides (duodecagon shaped) centred on a one-particle trajectory under the influence of a magnetic field. Leaving the inner Lagrangian point  $L_1$ , the motion is initially purely ballistic and the trajectory bound to the orbital plane. Later the matter connects to the magnetic field of the white dwarf.

The azimuth of the threading point is determined by the centre of the optical/X-ray absorption dip in the light curve of HU Aqr, just preceding eclipse. This dip is caused by the magnetic part of the stream close to the threading region crossing the line of sight to the white dwarf. From the threading region onwards, the stream is assumed to follow a dipolar field line.

The geometry of the non-transparent stream is shown in Fig. 1. Pixel 1 is always facing “upwards”, i.e. the surface normal of pixel 1 is parallel (in the ballistic stream) or closest to the orbital axis (in the magnetic stream). The area normal of pixel 4 is pointing *outwards*, that of pixel 10 *inwards* with respect to the white dwarf. At any given time, maximally half the pixels can be seen by the observer. However, the identity of the visible pixel change with orbital phase. This justifies the use of the *full observed light curve*. In eclipsing system like HU Aqr, the pixels are additionally occulted by the secondary during a short phase interval.

The length of the trajectory is divided into 110 parts of equal length, hence our resulting maps will have  $12 \times 110$  pixels. For simplicity, the eclipse of the rising part of the magnetic stream by the falling part, a short-time event, and vice versa is not included.

The phasedependent (integrated) flux  $F_{\nu,\varphi}$  at frequency  $\nu$  in the light curve is calculated from the map as:

$$F_{\nu,\varphi} = f(d) \sum_{j=1}^M (I_j v_{j,\varphi} a_{j,\varphi}) \quad (1)$$

where  $f(d) = 10^{26} R_{L1}^2/d^2 \cos i$  is a scale factor depending on the distance  $d$  and the size of the system expressed as  $R_{L1}$  in cgs units, as well as including a conversion from intensity to flux units (factor  $10^{26}$ ) and the inclination angle  $i$ .  $I_j$  is the intensity at the pixel  $j$  in the stream,  $M$  the number of pixel,  $v_{j,\varphi}$  the occultation function,  $a_{j,\varphi}$  the projected area of the pixel and  $\varphi$  denotes the orbital phase.

The data are fitted according to the maximum entropy method (MEM, Skilling & Bryan 1984) by minimizing the quality function  $Q$  (Horne 1985, Bryan & Skilling 1984):

$$Q = \frac{1}{N} \sum_{\varphi=1}^N \left( \frac{f_{\varphi} - F_{\varphi}}{\sigma_{\varphi}} \right)^2 - \alpha S \quad (2)$$

where  $f_{\varphi}$  is the observed flux,  $p_{\varphi}$  the predicted flux,  $\sigma_{\varphi}$  the uncertainty of the observed flux and  $N$  the number of data points in the light curve.  $S$  is a quantity describing the entropy of the intensity distribution along the stream and calculated as

$$S = \sum_j I_j - D_j - I_j \ln \frac{P_j}{D_j} \quad (3)$$

where  $D_j$  is the so-called *default* image calculated as a smeared out version of the actual image  $I_j$  and  $\alpha$  is the Lagrange multiplier. In ASM the smearing of the *default* image is performed in two dimensions, i.e. around and along the stream tube. The chosen way of smearing is the only sensible one. Imagine a spot on the stream, then it can be apparently smeared out due to optical depths effects around the stream and/or smeared along the stream due to the motion of the material in the stream.

MEM uses the information of the gradients to find the minimum of the quality function  $Q$ . The criterion to stop

iterating is defined by convergence, i.e. when the gradients corresponding to the  $\chi^2$  and the entropy  $S$  are antiparallel. In a rough picture, this ensures us of being in the entropy- $\chi^2$ -parameter space right inbetween the maximum of entropy and the minimum of the  $\chi^2$ . A further explanation of this convergence criterion can be found in Bryan & Skilling (1984) and Horne (1985).

MEM guarantees that the solution we retrieve is the simplest, but still compatible with the observations. However, there is no guarantee that we always find the global minimum and do not end up in a local minimum with little chance to escape from it. To ensure a minimum of prejudice and allow comparison of different maps, the inversion process was always started with an absolute flat, homogeneous map. The reconstructions of artificially produced maps (as done in Section 3.3) helps us to learn the behaviour of the method.

### 3.2 The system parameters

The geometry of the stream and our aspect on it are determined by five parameters: the mass ratio  $Q = M_{\text{wd}}/M_2$ , the orbital inclination  $i$ , the orientation of the magnetic axis (co-latitude  $\delta_{\mu}$ , azimuth  $\chi_{\mu}$ ) and the azimuth  $\chi_{\text{th}}$  of the threading region. All these parameters are reasonably well determined from optical and X-ray photometry and spectroscopy. We have checked, that the remaining uncertainties in these parameters do not affect our results. All azimuthal angles are measured in a reference system centred on the white dwarf with respect to the line joining both stars. The inner Lagrangian point  $L_1$  has  $\chi = 0^\circ$ , the accretion stream is deflected to negative azimuths.

Unpublished spectroscopy of photospheric Na-lines from the secondary star shows that the mass ratio must be higher than  $Q > 3.5$ . We adopt  $Q = 4$  throughout our analysis. The optical eclipse width then constrains the inclination to  $i = 85.6^\circ$ .

The X-ray bright phase of HU Aqr as observed with ROSAT in a high accretion state in October/November 1993 is centred on phase  $\phi_{\text{ecl}} = 0.875$ . Assuming that the azimuth for the accretion spot  $\chi_{\text{spot}}$  and the dipolar axis  $\chi_{\mu}$  are the same, this allows us to derive the azimuth of the magnetic axis to  $\chi_{\mu} \simeq \chi_{\text{spot}} = -45^\circ$ . Optical and X-ray light curves show a pronounced pre-eclipse dip centred on  $\phi_{\text{ecl}} = 0.880$ . The dip is caused by absorption of radiation from the white dwarf in the magnetic stream. Since HU Aqr is a high-inclination system, the phase of the dip indicates the azimuth  $\chi_{\text{th}}$  of the threading region,  $\chi_{\text{th}} \simeq -43^\circ \simeq \chi_{\mu}$ . The magnetic co-latitude of the dipolar axis finally was derived by SMH97 and Heerlein et al. (1999) to be of the order  $10^\circ - 15^\circ$ .

It was mentioned already in the introduction, that an accretion curtain is likely present in HU Aqr. This was derived by SMH97 from the observed shielding of the leading hemisphere of the secondary star from X-ray irradiation. The curtain is expected not only to absorb continuum radiation, but also to emit line radiation. The adoption of a stream instead of a curtain is therefore oversimplified, but unavoidable due to the one-dimensionality of the input data. We tried to map the observed brightness distribution also on a simple accretion curtain with the result, that the intensity is not distributed over the full curtain (as expected),

but that only some curious pixel become bright. Mapping on a full curtain is therefore more complicated and requires to take e.g. velocity information into account.

### 3.3 Application to artificial data

In order to evaluate how well our new method can reconstruct the stream emission, we tested it on artificial data. For that purpose we computed artificial intensity distributions, calculated the corresponding light curves and reconstructed the initial intensity distributions by ASM. From the deviations between the reconstructions and the original intensity distributions we learn about the behaviour of the algorithm, its power and limits.

#### 3.3.1 Tests for different spot locations

For these tests we used the same stream and viewing geometry as for the real data of HU Aqr as explained in the previous Section. We created three different artificial stream maps, each with a spot on the inner side of the stream (pixel row 10), but different locations along the stream. In the first case, the spot is located in the middle of the ballistic part of the stream, in the second case at the threading region and in the third case on the magnetic part of the stream. Outside the spot, the intensity was set to a constant level of 10% of the spot intensity. For these artificial pixel patterns (Fig. 2, top row) we calculated the light curves with the same phase resolution (and distribution) as in the observed data and added artificial noise with a signal-to-noise (S/N) of 100 (Fig. 2, middle row) plus a constant error, to avoid vanishing errors at mid-eclipse. These synthetic data were then analysed with ASM (Fig. 2, bottom row).

The synthetic light curves are determined by the folding products of the phase-dependent visibility and the foreshortening functions of each pixel. These are then summed over all pixels for a given phase. Consequently, the models with spots on the ballistic part of the stream do not show any difference in the phase interval  $\simeq 0.55 - 1.00$ : at these phases the spot is invisible for the observer ( $i \simeq 85^\circ$ ). Differences exist between these two light curves at egress phase, where the light curve of the model with the spot closer to the  $L_1$ -point shows a more pronounced step-like behaviour, and for the phase of the primary maximum. This maximum appears latest in the binary cycle for the model with the spot closer to  $L_1$  which is the natural consequence of the curvature of the trajectory: the observer has to move by the largest angle around the binaries axis until the optimum projection angle for the region with the bright spot is reached.

The third model with the spot on the magnetic part of the stream differs at all phases from the first two models: its eclipse light curve is much more symmetric than those of models '1' and '2'; the primary maximum appears at earliest phase; the ingresses to the primary and secondary minima show each a bend not present in the other two light curves; and the contrast between the primary and the secondary maximum is reduced.

In the bottom row of Fig. 2 we show gray-scale images of the reconstructed intensity distributions. The *location of the spot* is in each case reconstructed very well, the spots are only smeared out due to the MEM algorithm, leading to a different spot profile and lower spot intensity.

We find some low amplitude structures near the secondary star on the outer side of the stream (circumference pixel 1 – 7, length pixel  $< 50$ ). These structures were probably introduced due to fitting noise in the ingress phase, the only phase when this region is visible. If we see such structures in reconstructions of real light curves, they might be caused similarly and therefore have to be treated as artefacts.

#### 3.3.2 Tests with lower quality data

Additionally, we tested the method for lower phase resolution, a lower signal-to-noise ratio and a missing eclipse coverage as shown in Fig. 3.

For the first test with low quality data we set the phase resolution simply to twice as low as that in the first test cases by using only every second phase value. This especially affects the egress phase which already has a low phase resolution. Nevertheless, we can recover the spot very well and in general is the reconstruction little different from the one in Fig. 2 (middle bottom). The only difference is an enhancement of artefacts, e.g. the low amplitude structures near the secondary star (see above). Even with a phase resolution of only 20 data points during the full orbit could we recover indication of the spot, however, severely smeared out around the stream.

In the second of these tests we set the signal-to-noise ratio artificially to a value of 10, i.e. ten times lower as for the tests in Fig. 2 and comparable to the signal-to-noise ratio in the HU Aqr data. The constant additional error was also set a factor of 10 higher than in the other test cases. Still, we recover the spot very well and the reconstruction differs only in terms of, though strongly, enhanced artefacts near the secondary (as described above) and on the magnetic part of the stream.

In the third of these test cases we used the same phase resolution and phase coverage as in Fig. 2 (middle middle), but cut out the fluxes between phases  $-0.1$  and  $0.1$ . Additionally, we used here a S/N of 20 instead of 100, as in most other test cases. Even if the eclipse is not covered by observation, we can still see indication of the spot at the threading region, however very weak and smeared out along and around the stream. The artefacts seen in all other test cases disappeared, indicating that the data points around the eclipse are truly responsible for them. The lower signal-to-noise ratio does not have any large effect on the reconstruction, the maps for S/N = 100 and S/N = 20 look very similar. This test shows very well, how the out-of-eclipse light curve is determined by the emissivity of the stream. While the eclipse profile gives details and sharper contrasts in the maps, the general behaviour of the outside eclipse light curve provides us with information on the general features in the stream emissivity: the difference in maxima at phases  $-0.25$  and  $0.25$  indicate which side of the stream is brighter and the shape of the (brighter local) maximum (spanning about a third of the orbit) indicates, where the spot is (cf. also the light curves in Fig. 2). This information is little influenced by flickering or a low signal-to-noise ratio.

These tests show that our new method is very robust and can recover the general features of the original intensity distribution even from lower quality data. *This is due to the use of the full light curve.* Of course, the quality of the

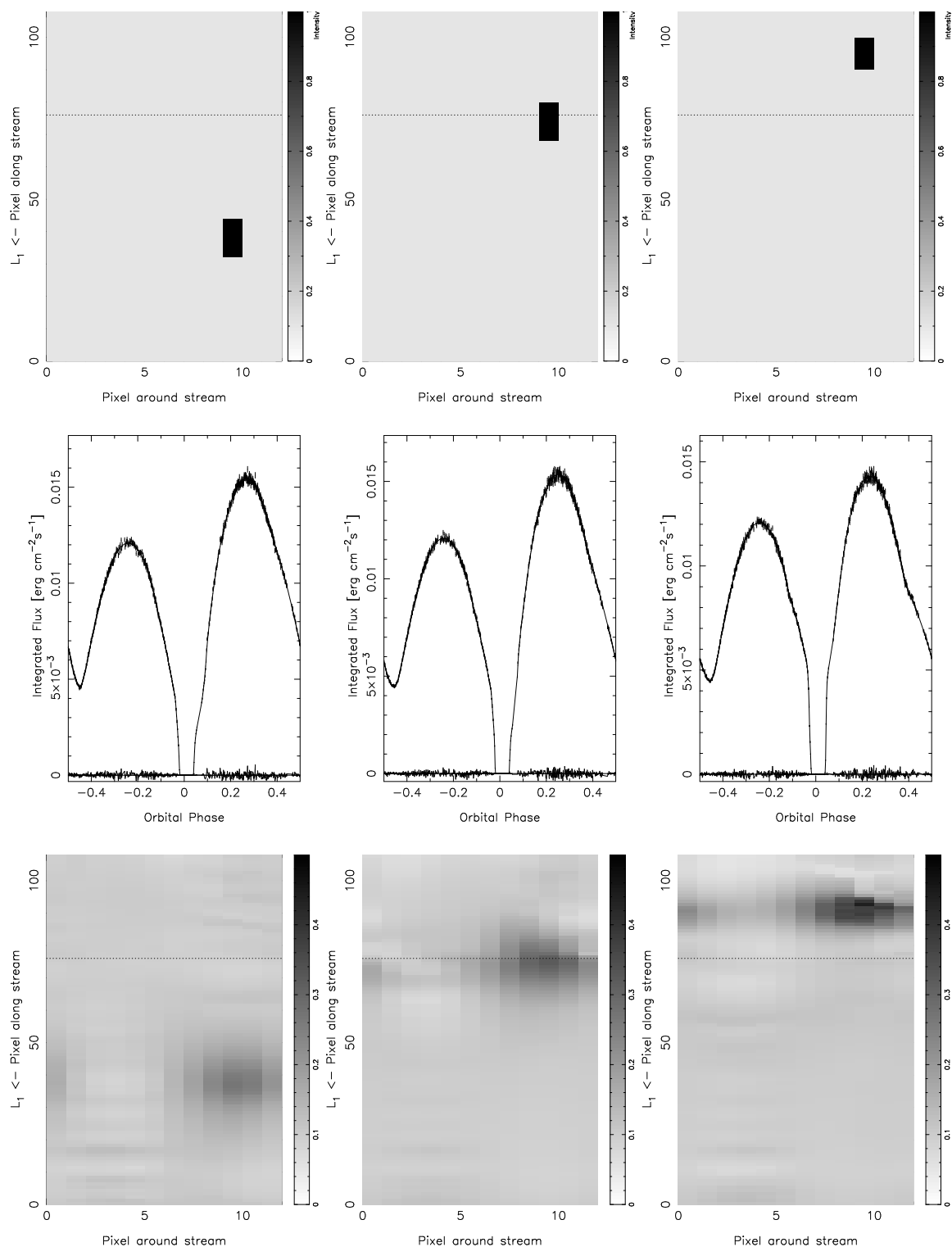


**Figure 2.** Test of ASM for different spot locations using artificial data: Shown are the input maps (top), the original and reconstructed light curves (middle) and the reconstructed maps (bottom). The maps have the pixel-coordinate around the stream along the abscissa (according to the convention shown in Fig. 1) and the pixel-coordinate along the stream at the ordinate. The horizontal dashed line corresponds to the threading region. On input, a constant intensity distribution with a bright spot located on the ballistic stream (left), the coupling region (centre), and the magnetic stream (right) has been assumed. Noise has been artificially created with a signal to noise of 100 and added to the data before reconstruction.

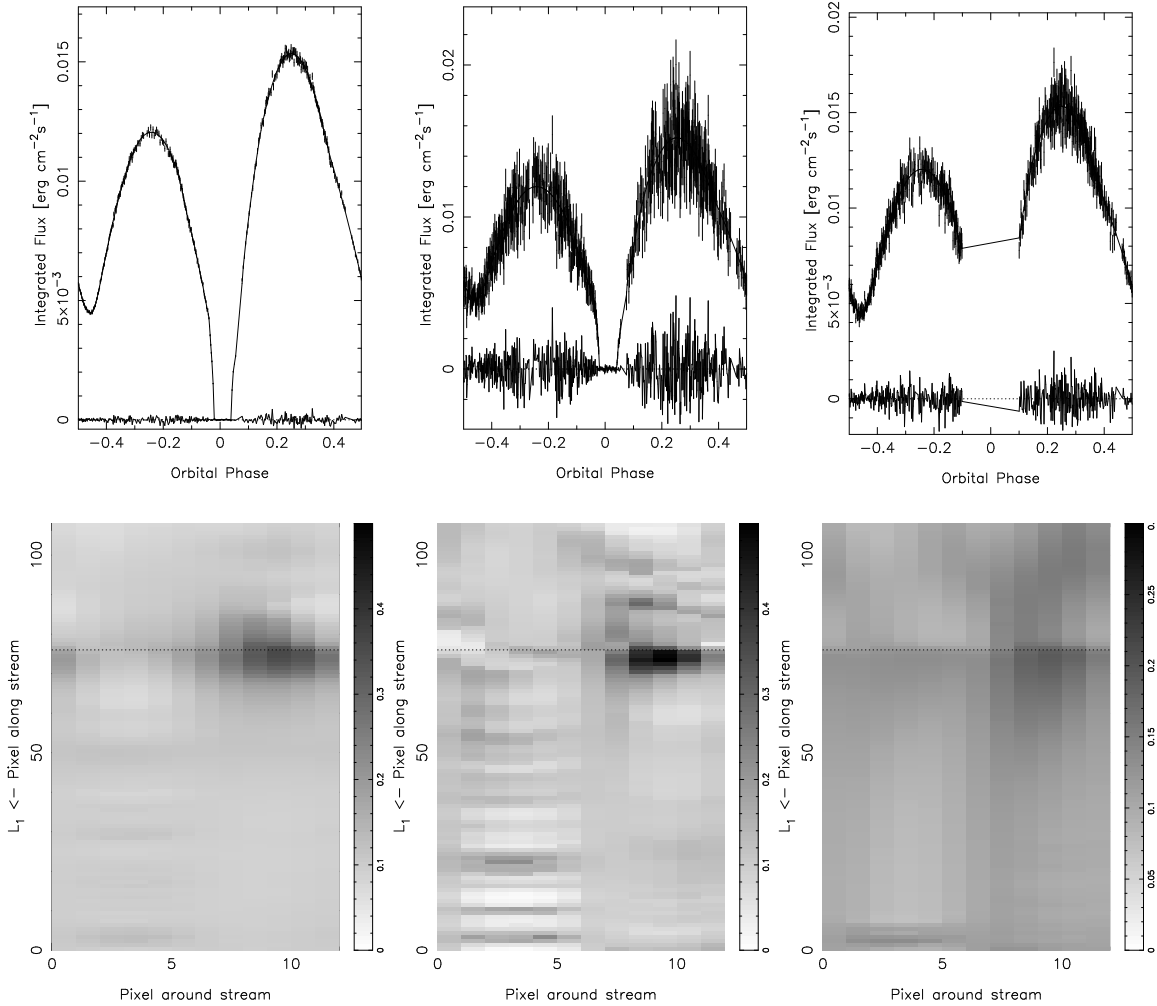


**Figure 3.** Test of ASM with lower quality data: using a twice as low phase resolution (left), a ten times as low signal-to-noise ratio ( $S/N=10$ ) (middle) compared to Fig. 2 and a missing eclipse coverage (right; the line in the light curve across the eclipse simply connects the flux points at phases  $-0.1$  and  $0.1$ ). The input map is identical to the one in Fig. 2 (top middle) with a spot located on the coupling region. Shown are the original and reconstructed light curves (top) and the reconstructed maps (bottom). The maps have the pixel-coordinate around the stream along the abscissa (according to the convention shown in Fig. 1) and the pixel-coordinate along the stream at the ordinate. The horizontal dashed line corresponds to the threading region.

reconstructions depends on using the right geometry for the stream. This is shown in test reconstructions in the following Section.

### 3.3.3 Tests for the stream geometry

Furthermore, we tested the ASM method against choosing wrong parameters for the stream geometry. For these tests we used the light curve in Fig. 2 (middle, middle) and reconstructed the intensity distribution assuming slightly wrong parameters for the mass ratio, the azimuth of the threading region (determined by the magnetic field strength), the colatitude and the azimuth of the dipolar axis.

In the test case where we chose an azimuth of the threading region smaller by about  $8^\circ$  (i.e. a magnetic field strength smaller by about 15%) the magnetic part of the stream also becomes shallower, changing the geometry quite dramatically. For this test case we cannot find any converged solution, not even for an as high  $\chi^2$  as 10. The intermediate, unconverged map shows artefacts in form of pixel-to-pixel

variations. This means the azimuth of the threading region is very well defined.

Similar is the behaviour of the reconstruction process when we choose a false mass ratio. For the test case we used  $q = Q^{-1} = 0.3$ . It changes the stream geometry in a similar way as in the previous test case, however in the opposite direction. Again we could not find a converged solution for even a  $\chi^2$  of 10. The intermediate unconverged maps show again strong artefacts, however, indication for the spot at the right location.

If we change the colatitude of the magnetic axis, it mainly changes the spatial amplitude of the magnetic part of the stream. A value smaller by  $5^\circ$  leads already to a 10% increase in deflection. The resulting map (Fig. 4) still shows the spot, but also an additional bright spot at the *inner* side of the magnetic part of the stream and a dark spot on the *upper* side. While this alone would not allow us to dismiss the geometry, the pixel-to-pixel variation around the second spot and enhanced artefacts on the ballistic part of the stream indicate that we chose a false geometry. The appear-

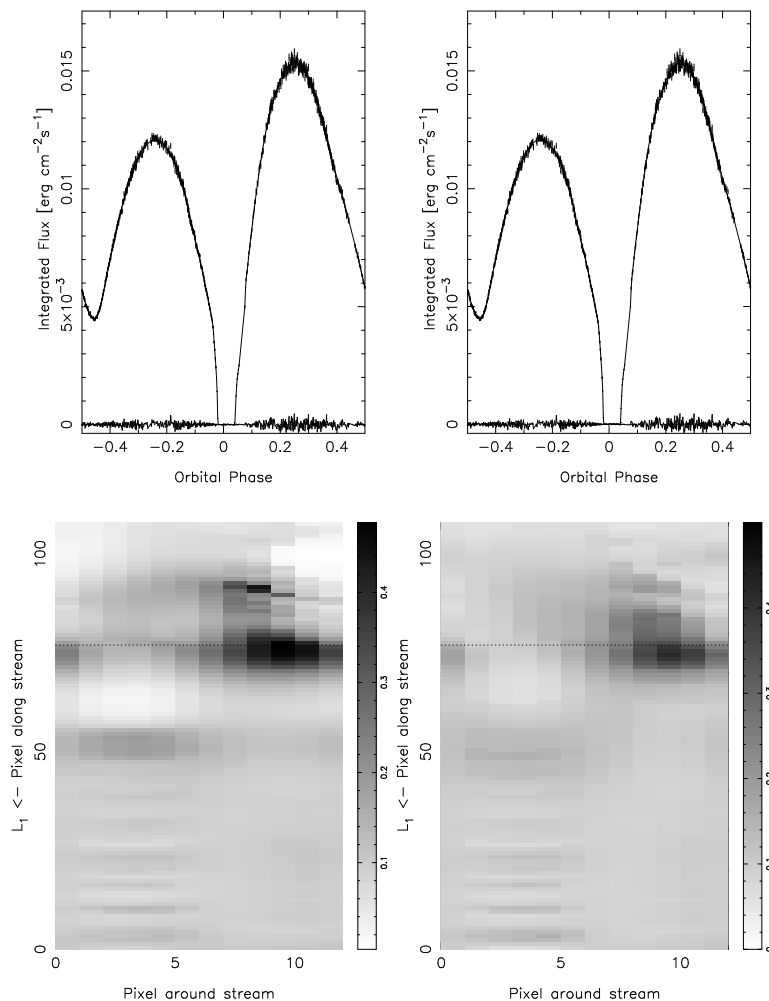


**Figure 4.** Test of ASM for the stream geometry: using a too small colatitude (left) and a too small azimuth (right) of the magnetic axis. The input light curve is identical to the one in Fig. 2 (middle middle) created from a map with a spot located on the coupling region. Shown are the original and reconstructed light curves (top) and the reconstructed maps (bottom). The maps have the pixel-coordinate around the stream along the abscissa (according to the convention shown in Fig. 1) and the pixel-coordinate along the stream at the ordinate. The horizontal dashed line corresponds to the threading region.

ance of this second spot is understandable: the reconstructed intensity distribution on the magnetic part of the stream for the too strongly deflected stream path is asymmetric in an attempt to reproduce the true intensity distribution of the shallower stream path. Bright or dark spots around the spatial maximum of the stream path should therefore be interpreted cautiously. They can be introduced by wrong geometry parameters.

The azimuth of the magnetic axis is much less well defined than the other geometry parameters. Only for an angle different by more than  $30^\circ$  we could see a significant change in the deflection in the magnetic part of the stream (and a shift in the location of the maximum of spatial deflection). The map with the reconstructed intensity distribution as shown in Fig. 4 therefore shows not very extreme differences to the one in Fig. 2 (middle bottom), but also indication for a second spot on the magnetic part of the stream and enhanced artefacts.

These tests show that the geometry of the system is relatively well defined. In case we choose false geometry parameters (especially false values for the magnetic field or the

mass ratio) the reconstructions show artefacts and pixel-to-pixel variations. Such structures will give us some indication for the goodness of the geometry parameters from the final reconstructions. If on the other hand a geometrical parameter is less well defined (as the azimuth of the magnetic axis), it does not influence the map to a great extent and the general features are reconstructed very well.

### 3.4 Application to *HU Aqr*

#### 3.4.1 The light curves

The light curves of the three emission lines, corrected for the contribution of reprocessed light from the secondary star, are shown in Fig. 5 (top row). They are very similar in shape, showing the total eclipse around phase zero, a secondary minimum at phase  $\sim 0.55$  ( $\equiv -0.45$ ), a primary maximum at phase  $\sim 0.24$ , and a secondary maximum at phase  $\sim 0.74$  ( $\equiv -0.26$ ). The major difference between the light curves of Hydrogen and Helium is the lower contrast between the primary and secondary minima for the line of ionized He-

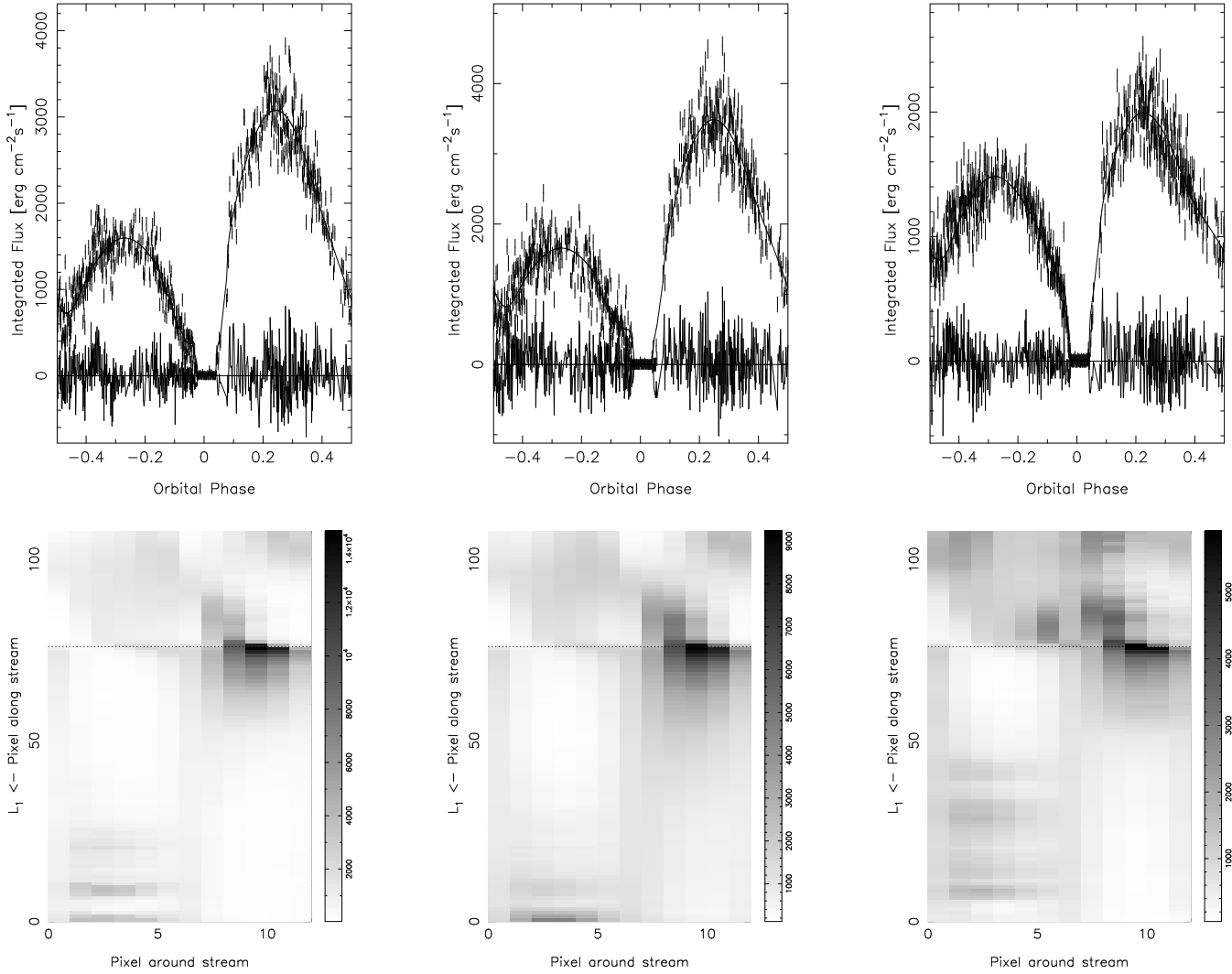


**Figure 5.** *Top row:* The light curves of  $H\beta$ ,  $H\gamma$  and  $He\ II\ \lambda 4686$  as analysed, i.e. corrected for the contribution of reprocessed light from the secondary, together with the fits (solid line through observed data) and the residuals (solid line around flux 0). *Bottom row:* The reconstructed intensity distributions on the surface of the accretion stream as gray-scale plots. The horizontal dotted line at pixel 76 denotes the threading location.

lium. The sampling of the light curves is sparse in the phase interval 0.05 – 0.08, i.e. at phase of eclipse egress.

ASM was applied to these light curves and their overall shape was reconstructed very well, except for some details of the eclipse profiles (see below). ASM tries to fit a given light curve until some predefined value of  $\chi^2 = \sum((f - p)/\sigma)^2$  (where  $f$  and  $p$  are the observed and predicted data, respectively and  $\sigma$  is the uncertainty of the observed data points) is reached. Since the data points around eclipse are not very numerous, they do not affect the general solution substantially. The choice of the  $\chi^2$ 's obviously introduces some kind of subjectivity. Our choice was driven by the two opposing constraints to reach an as good as possible fit to the light curves and not to introduce too many (most likely artificial) structures into the maps. Our finally chosen values of  $\chi^2 = 4$  for the Helium line and 7 for the Balmer lines appear somewhat high. However, this choice was necessary due to the rather large scatter of the individual data points due to flickering and flaring in the lines and possibly small deviations of the true stream geometry from the one we used.

For lower  $\chi^2$ , artefacts due to overfitting were dominating the maps.

The fitted light curve at the given  $\chi^2$ -level is shown as solid line in each panel of Fig. 5 with the same phase sampling as the input data. The solid line scattered around zero intensity in each panel indicates the residuals of the data points with respect to the fitting solution. The residuals mainly show a random scatter with an exception around eclipse phase, where the residuals are systematically negative. Unfortunately, at egress, just where the fit to the data would be especially important, the data are only poorly sampled.

### 3.4.2 The maps

The reconstructions of all three emission lines clearly show a bright spot in the threading region on that side of the stream which faces the white dwarf. Otherwise, the intensity of the ballistic stream is low, not unlike our test stream. The wave-like intensity pattern in the lower left region of



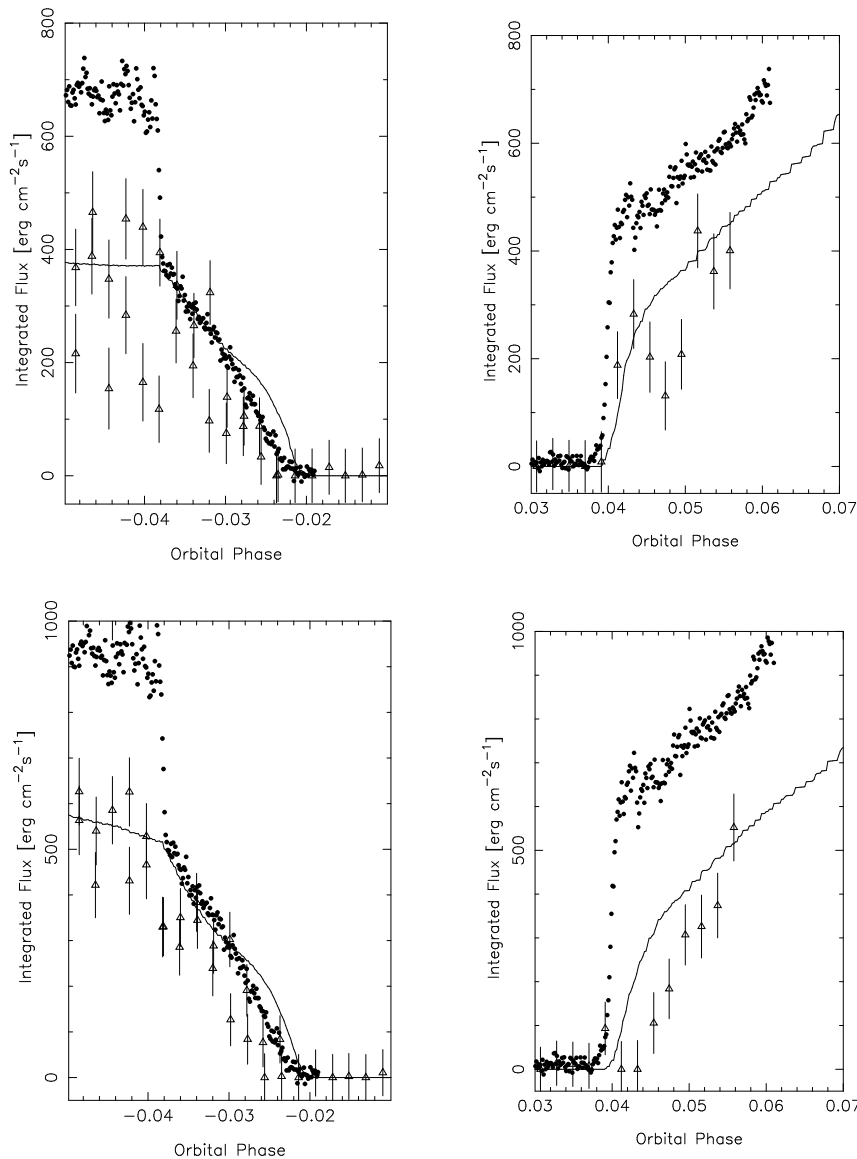


**Figure 6.** Details of the light curves in  $H\beta$  (top) and  $He\ II\ \lambda 4686$  (bottom) at eclipse ingress and egress, respectively. Shown are the integrated fluxes in the emission lines (triangles with error bars), the ASM-based fits to the light curves, the same as in Fig. 5 (solid lines), and the broad-band  $B$  light curves (filled circles).

the maps, i.e. near the  $L_1$ -point on the non-illuminated side of the stream (circumference pixel  $< 7$ , length pixel  $< 30$ ) is interpreted as numerical artefact (see Section 3.3).

The fits show a migration of the maximum intensity from pixel '10' in the threading region, where the ballistic stream is irradiated from the side towards pixels '9' and later '8' in the magnetic part. In the twisted part of the stream around the threading region these are the pixel facing the white dwarf most perpendicularly, i.e. would receive most irradiation. These pixel being so bright is therefore compatible with a direct irradiation from the hot accretion spot where the ionizing source can be located.

### 3.4.3 Detail in the light curve

Details of the light curves and the light-curve fits at eclipse ingress and egress are shown together with simultaneous

MCCP B-band photometric data in Fig. 6. The MCCP data were scaled by an appropriate factor so that the ASM-based fits and the MCCP data agree with each other at the initial ingress phase (phase  $\simeq -0.038$ ). When comparing the two types of data, one should bear in mind, that they consist of somewhat different radiation components: The spectroscopic data contain only radiation from the emission lines originating in the accretion stream. This radiation is considerably optically thick. The MCCP data contain as well the recombination continuum which is likely to be optically thin. Outside the white dwarf's eclipse, additional radiation from the undisturbed and accretion-heated photosphere of the white dwarf and cyclotron radiation from the accretion plasma is contained in the broadband data recorded with the MCCP. Hence, we cannot expect to see exactly the same shapes of the emission line and broadband photometric light curves. However, these data with their high time resolution

allow a detailed comparison of the contact times and thus provide as with a test if our overall geometry is chosen correctly.

First of all, the contact phases (however, not the egress slopes) of the two MCCP-data and the ASM-fit agree with high precision. For that comparison one must not take notice of the initial steep steps at eclipse ingress and egress in the MCCP-data, which are due to the occultation of the white dwarf. The precursor seen in the MCCP-data immediately before the steep rise at egress,  $\phi = 0.037 - 0.039$ , is due to the non-heated photosphere of the white dwarf emerging from eclipse. The spectroscopic data set and the model do not contain radiation from the white dwarf surface, therefore, the egress in the corresponding light curve is shallower and sets in at that phase, when the spot reappears behind the companion star. The contact time in the H $\beta$  light curve is consistent with the MCCP and ASM light curves, whereas the HeII light curve seems a bit late. We do not regard this as a serious inconsistency. The reader shall be reminded, that each spectroscopic data point shown in Fig. 6 represents a single spectrum of integration time 15 sec. The errors represent statistical errors only and do not account for calibration uncertainties and the background subtraction. A further source of uncertainty is introduced by the continuum subtraction which reveals slightly different results for the line fluxes if either a local or a global continuum is fitted and subtracted. The points of contact can be compared reliably only between the model and the MCCP-data and these agree quite well which gives us confidence in our choice of geometry and system parameters.

Secondly, as mentioned earlier, the emission line light curves carry less flux during stream ingress and egress than predicted by ASM. We have no final explanation for this disagreement. We cannot completely exclude a measurement error since only a few spectra were obtained particularly at eclipse egress. Also, our assumption of complete optical thickness might be a too strong requirement. Furthermore, the stream almost certainly has a more complex geometry than being a tube. SMH97 have shown that an accretion curtain exists and its existence must have an effect on the light curves. Such structures are probably best identified around eclipse. They do not necessarily alter the contact times, the most crucial one being that at  $\phi = -0.023$  which marks occultation of the outer envelope of the accretion stream/curtain. But they influence the overall brightness and the gradient of the light curve. If not a measurement error, we must conclude from the described discrepancy that mapping experiments using eclipse light curves alone will predict too high emission line fluxes outside eclipse.

Thirdly, ASM predicts a bend of the eclipse light curves, most pronounced at  $\phi = -0.025 = 0.975$  and  $0.045$ . Such bends are not observed with the MCCP and it is difficult to determine, whether such structure in the spectroscopic data set exists. With our assumed stream geometry, the last structure visible at ingress phase before being obscured by the companion star, is the unirradiated side of the threading region. This side of the stream does not show a bright spot like the irradiated side. The sudden decrease of light predicted by the ASM-fit after phase 0.975, is caused by the sudden eclipse of the, however, still relatively bright region on the stream. In contrast, the more gradual decline of the MCCP light curve might rather be indicating emission

from a more extended structure. As suggested in the preceding section, a structure like an accretion curtain, which cannot be modelled with the present one-dimensional data set, might be responsible for the discrepancy.

One should keep in mind, that the out-of-eclipse light curve is significantly determined by the stream emissivity and is little affected by the flickering and flaring or the low signal-to-noise ratio. Even though the exact shape of the ingress and egress light curves are not reproduced in detail and shape of this spot might not be exactly reconstructed, we regard therefore the presence of a spot at the threading region as highly likely.

#### 3.4.4 *The influence of the correction function*

Finally, we would like to discuss the influence of the correction function used for the contribution of reprocessed radiation from the secondary star (see Fig. 7 in SM97). First of all, the fits at eclipse phase are completely unaffected by the shape and scaling of the correction function because the intensity of that radiation component is zero at that particular phase interval. We investigated the influence of the correction function by using differently scaled correction functions of always the same shape (see Section 2). We scaled the nominal function by factors 1.5 and 0.5, respectively.

When scaling with a factor of 1.5 there is only little intensity left in the emission line light curves at phase 0.5. However, the effect on the resulting maps are minor. Using the same  $\chi^2$ -levels as for the fits in Fig. 3.4 the same bright spots in the threading region emerge where the spots are even more pronounced, i.e. less smeared.

If a scaling factor of only 0.5 is used (which is much less than the actual uncertainty is), the maps show enhanced brightness on the magnetic part of the stream on its outer side (pixel 2 – 6). This is easily explained: this part of the magnetic stream is best visible around phase 0.5, when also the irradiated hemisphere of the secondary star is best visible. Since our code does not account for the surface of the secondary star the stream apparently emits excess radiation at phase 0.5. This excess radiation is projected onto the outer magnetic stream, a physically unlikely location.

## 4 DISCUSSION

### 4.1 *The bright spot on the accretion stream*

Our ASM-code predicts a bright spot of line radiation in the threading region, where the stream is redirected and couples to magnetic field lines. This implies that X-ray/EUV irradiation alone is seemingly not the major source of excitation and ionization, but the combination of irradiation plus dissipative heating seems to be able to do the job. To our knowledge, this is, together with the work by Hakala (1995) and Harrop-Allin et al. (1998), the first direct proof of the prediction made further back in past by Liebert & Stockman (1985), that dissipation in the threading region occurs and has observational consequences. However, their prediction of X-ray emission from the threading region is still missing and can be proven only by XMM-observations of eclipsing polars.

A similar bright spot as in our brightness maps was

also found by Hakala (1995) in observations of *HU Aqr* in a low accretion state. Apart from that, Hakala reports a pronounced brightness increase towards the white dwarf. In their analysis of the 1993 high state *UBVR* light curves, Harrop-Allin et al. (1998) found the ballistic stream to be bright near the  $L_1$ -point and faint in the threading region. Just after the threading region towards the white dwarf, they observed a sudden brightness increase in all four colours. In contrast, their 1999 mapping analysis (Harrop-Allin et al. 1999b) of the same data shows an overall faint ballistic stream except for a bright spot near the threading region. As their one-footpoint stream leaves the orbital plane it fades and re-brightens again as it approaches the white dwarf. The reason for their picture changing so dramatically (as far as the ballistic stream is concerned) is a change of their global optimization scheme. Since their more recent analysis shows results closer to ours, we regard this as the more likely solution. Our and their analysis of different data sets taken only a few days apart show commonly the stream to be bright in the threading region. However, Harrop-Allin et al. used a restricted data set centred on the white dwarfs eclipse. This, together with the simplifying assumption of constant cyclotron and photospheric brightness out of eclipse, are the likely reasons for the differences in the resulting maps.

#### 4.2 The optical depth in the stream

In our approach the stream is assumed to be completely optically thick in the lines. This approach is supported by the fact that the observed emission line light curves show two distinct maxima at those phases when the largest surface of the stream is offered to the observer.

A comment concerning the recent work by Harrop-Allin et al. (1999b), which appeared after submission of the first version of our paper: They used broad-band data observed quasi-simultaneously with our spectroscopic data and mapped the brightness on a one-dimensional accretion stream. They also assumed optically thick radiation, even in the continuum. However, in their maps they assign only one brightness value to a certain pixel along the accretion stream. Both ingress and egress were used, where either the irradiated or the unirradiated side of the stream is seen. As it is clear from our emission line light curves and from our maps, the stream has different brightness on both sides. In this respect the approach by Harrop-Allin et al. (1999b) is insufficient.

Along the same line, ASM has also an advantage over Doppler tomography: in Doppler tomography one implicitly assumes that the emission is optically thin. Therefore, no information about different emissivities from the irradiated and non-irradiated sides can be obtained from the Doppler maps.

Furthermore, our ASM approach has the advantage of using the maximum information in the form of the full orbital light curve. Using emission line data, we exclude explicitly emission from the white dwarf and the accretion spot. This offers a much more undisturbed and cleaner view onto the accretion stream. Our presented analyses suffers, however, from the few photons available around eclipse phase, where – at least in principle – crucial tests of the stream geometry and brightness distribution were possible.

#### 4.3 The luminosity balance of the stream

As mentioned earlier, Hakala’s and Harrop-Allin et al.’s maps show dominating brightness in the magnetic part of the stream close to the white dwarf. Fig. 6 shows, that the *B* band light curve displays a more gradual decline during ingress and egress than predicted by ASM. These observed profiles may be caused by a brighter magnetic stream than our mapping experiment predicts but may also be due to a bright accretion curtain or a similar more complicated geometric structure.

However, we searched for independent information about the luminosity balance between the ballistic and the magnetic streams by analysing the observed emission line profiles directly. We used two approaches: in the first we calculated the integrated brightness in selected parts of the Doppler maps; in the second we decomposed the line profiles at appropriate phases into subcomponents. Both approaches rely to a large extent on the assumption that the observed structures in the Doppler maps and in the spectral lines can be assigned to physically different locations in the binary system.

In the Doppler maps three distinct structures can be associated to the irradiated secondary star, the ballistic stream and the magnetic stream (SMH97, Figs. 11, 12). The Doppler map of  $\text{He II } \lambda 4686$  suggests that about one third ( $\sim 30\%$ ) of the total stream emission originates from its magnetic part.

Investigating the emission lines is somewhat more complicated: The parallel projection of a Doppler map at a given angle gives a spectrum (intensity vs. velocity, hence wavelength) at a certain binary phase, as observed in the line profile. The structure of the Doppler maps presented by SMH97 show clearly that no projection angle exists where the different structures can be separated uniquely into spectral features, i.e. without contamination by a another emission component. However, the separation between the ballistic and the magnetic parts of the stream seems to be most easily possible at phases 0.25 and 0.75.

At these phases, the ballistic stream is perpendicular to the line of sight to the observer. The velocity component we see as the radial velocity is  $v_y$  in the Doppler maps and which is relatively sharply defined. It can be read off from the Doppler map as  $v_y \simeq +190 \text{ km s}^{-1}$ . The magnetic stream occupies the region of the  $(v_x, v_y)$ -Doppler map with negative  $v_y$ -velocities, because at the given phases the radial velocities along the magnetic stream are antiparallel to those of the ballistic part. Hence, in the line profile at the given phases it occurs as a broad feature with opposite sign of its bulk velocity (opposite sign with respect to the ballistic stream). Even at these optimum phases the high-velocity tail of the ballistic stream overlaps with emission from the magnetic stream (in the parallel projection of the Doppler map). Therefore, a decomposition using Gaussian curves will result in an overestimate of the contribution from the magnetic stream. A Gaussian deconvolution of the spectral line profiles of  $\text{He II } \lambda 4686$  at the given phases reveals less than  $\sim 50\%$  emission from a broad base component. The percentage is somewhat lower for  $\text{H}\beta$ , namely  $\sim 45\%$ .

As expected, the fraction of flux in the broad base component (i.e. originating in the magnetic stream) is higher than the value derived from the measurement made in the

Doppler map, due to the superposition of different radiation components. We conclude, that observationally the contribution of light from the magnetic stream to the total brightness of the stream is certainly below 50%, but more likely of the order of 30%. The integrated brightness from the magnetic stream of our maps (Fig. 5) is  $\sim 40\%$  in He II  $\lambda 4686$  and  $\sim 30\%$  in the Balmer lines. We regard these numbers as support for our approach.

#### 4.4 Outlook

Clearly, for a better understanding of the brightness distribution along the different parts of the accretion stream and the accretion curtain one needs to take into account not only the light curve, but also the line profiles, i.e. combine the two methods *Doppler Tomography* and *Accretion Stream Mapping*. We plan to establish an *Eclipse Doppler tomography* as a future step of analysis. The necessary input data with high time and spectral resolution can be obtained utilizing 8m-class telescopes.

#### ACKNOWLEDGMENTS

We thank the referee for helpful comments. SV thanks the South African NRF (formerly FRD) for funding a postdoc fellowship and the AIP for kind hospitality in October 1997 and April 1999. This work was supported by DLR grant 50 OR 9706 8.

#### REFERENCES

- Hakala P.J., 1995, A&A, 296, 164  
 Heerlein C., Horne K., Schwope A.D., 1999, MNRAS 304, 145  
 Hameury J.-M., King A.R., Lasota J.-P., 1986, MNRAS 218, 695  
 Harrop-Allin M.K., Hakala P.J., Cropper M., 1999a, MNRAS 302, 362  
 Harrop-Allin M.K., Hakala P.J., Cropper M., Hellier C., Ramsayer T., 1998, ASP Conf. Ser. 137, 511  
 Harrop-Allin M.K., Cropper M., Hakala P.J., Hellier C., Ramsayer T., 1999b, MNRAS 308, 807  
 Horne K., 1985, MNRAS, 213, 129  
 Kube J., Gänsicke B.T., Beuermann K., 2000, A&A 356, 490  
 Liebert J., Stockman H.S., 1985, in *Cataclysmic Variables and Low-Mass X-Ray Binaries*, eds. D.Q. Lamb and J. Patterson, Reidel, Dordrecht, p. 151  
 Schwope A.D., Mantel K.-H., Horne K., 1997, A&A, 319, 894 (SMH97)  
 Skilling J., Bryan R.K., 1984, MNRAS 211, 111  
 Sohl K., Wynn G., 1999, ASP Conf. Ser. 157, 87  
 Vrielmann S., Schwope A.D., 1999, ASP Conf. Ser. 157, 93  
 Watson M.G., King A.R., Jones M.H., Motch C., 1989, MNRAS 237, 299